Pressure-induced *Pbca-P2₁/c* phase transition of natural orthoenstatite: Compositional effect and its geophysical implications

JIN S. ZHANG,[1,*] BRUNO REYNARD,[2] GILLES MONTAGNAC,[2] RU CHENG WANG,[3] AND JAY D. BASS[1]

[1]Department of Geology, University of Illinois, Urbana, Illinois 61801, U.S.A.
[2]Laboratoire de Géologie de Lyon, CNRS, Ecole Normale Supérieure de Lyon, 69007, France
[3]State Key Laboratory for Mineral Deposits Research, Department of Earth Sciences, Nanjing University, Nanjing 210093, China

ABSTRACT

Raman spectroscopy has been employed to investigate possible compositional effects on the high-pressure phase transition of Mg-rich orthoenstatite to a newly discovered $P2_1/c$ phase. Three natural orthoenstatite (OEN) samples were used in this study: near end-member Mg orthoenstatite (Zabargad Island, Egypt), Al-free, Fe-bearing orthoenstatite (Morogoro, Tanzania) and Al-rich, Fe,Ca-bearing orthoenstatite (Kilbourne Hole, New Mexico). Experiments were carried out at room temperature. For all samples, the high-pressure phase transition is characterized by a splitting of the 660–680 cm^{-1} doublet in the Raman spectrum into a triplet, with a corresponding change of peak intensities. These spectral changes are caused by the lowered symmetry of the high-pressure phase, as indicated by structural refinement from single-crystal X-ray diffraction results. The high-pressure phase of all samples appears to have space group $P2_1/c$. No evidence for a $C2/c$ phase was observed. Our results indicate that upon compression, the presence of 10 mol% Fe decreases the onset pressure of formation of the high-pressure $P2_1/c$ phase by about 1 GPa. Results for the Kilbourne Hole OEN show that upon compression, a combined enrichment of Al and Ca contents increases the onset pressure of formation of high-pressure clinoesntatite (HPCEN2) by over 3 GPa relative to Tanzania OEN. Upon decompression, all samples revert to single crystals of the orthoenstatite starting phase. Our measurements suggest that orthoenstatite is the prevalent phase of Mg-rich pyroxene throughout the uppermost mantle, whereas the newly discovered $P2_1/c$ phase might be present near the bottom of uppermost mantle, slightly shallower than the top of the transition zone.

Keywords: Orthoenstatite, high-pressure clinoenstatite, high-pressure phase transition, upper mantle, Raman spectroscopy

INTRODUCTION

Mg-rich, Fe-bearing pyroxene with approximate composition $(Mg,Fe)SiO_3$ is one of the major minerals in Earth's uppermost mantle. Four polymorphs of $(Mg,Fe)SiO_3$ are potentially stable under upper mantle conditions: orthoenstatite (OEN) with space group *Pbca* (Morimoto and Koto 1969), low-pressure clinoenstatite (LPCEN) with space group $P2_1/c$ (Morimoto et al. 1960), high-pressure clinoenstatite (HPCEN) with space group $C2/c$ (Angel et al. 1992), and a newly discovered high-pressure monoclinic polymorph (HPCEN2) also with space group $P2_1/c$ (Zhang et al. 2012). Although the equilibrium stability fields for these four polymorphs have not yet been firmly established, the discovery of the new $P2_1/c$ structure has potentially important implications for the phase relations in the $(Mg,Fe)SiO_3$ system and for upper mantle mineralogy.

Experimentally determined pressures for the transition from OEN to the high-pressure polymorph HPCEN2 span a wide range for different experiments using different samples with different techniques. For example, Raman spectroscopy on synthetic flux-grown $MgSiO_3$ (containing minor amounts of Li, Mo, V), compressed in a diamond-anvil cell (DAC), indicates a transition pressure of between 6.1 and 12.0 GPa in an argon pressure-trans-

mitting medium (Chopelas 1999), and between 9.5 and 10 GPa in water (Lin 2003). Multi-anvil ultrasonic experiments constrained the transition pressure to be between 9.6 and 11.8 GPa (Kung et al. 2004). For natural orthoenstatite from San Carlos, containing 8 mol% Fe and 2.5 wt% Al, the transition does not occur until 14.26 GPa in a neon pressure medium, as determined from single-crystal X-ray diffraction experiments (Zhang et al. 2012). For orthoenstatite from Kilbourne Hole, containing 9 mol% Fe and 5 wt% Al, there is no evidence for this phase transition up to 12.5 GPa by stimulated light scattering in a DAC (Chai et al. 1997). These discrepancies on the transition pressure suggest that chemical composition (both natural cation substitutions such Al, Fe, Ca, as well as the incorporation of artificial flux components such as Li, Mo, V), as well as the pressure medium used, could all have a significant effect on the transition pressure and possibly the phase relations between OEN, HPCEN LPCEN, and HPCEN2. Thus, it is important to separate the effects of chemistry from effects of the pressure medium to investigate the effect of composition on the stability of the $P2_1/c$ phase. Moreover, orthoenstatite in Earth's mantle does not exist as $MgSiO_3$, but will almost certainly contain Fe, Al, and Ca as minor elements, with the exact composition dependent on depth. In general, the Fe content of OEN tends to be relatively constant with increasing depth, whereas Ca and Al content will likely decrease as enstatite

TABLE 1. Comparison of Raman frequencies from previous studies

OEN, ambient condition							HPCEN2, normalized to 12.5 GPa				
Stalder et al.	Huang et al.	Lin	Chopelas	This study			Lin	Chopelas	This study		
(2009)	(2000)	(2003)	(1999)	Zabg	Tan	KBH	(2003)	(1999)	Zabg	Tan	KBH
		83	83				94.7	94.9			
		106.8					135.9	139.1			
		115.4	115				166	*168.8*	**168.3**		
133.8		**134.3**	134	**137.4**			174.6	178.1	*179.7*		
		155.3	153		155.7	*151.4*	183				
		161.5				160	196.4	197.5	**199.2**	195.7	
		166.7	166	**170.2**	169.3	169.7	204				
				190.1	190.9		224.4	225.5	**227.9**	**223.7**	223.8
197.5		196.9	197	196.5	**197.1**	**193.7**	231.8				
				201.1			250.5	251.7	**254.4**	**251.7**	**251.3**
206.4				**208.3**			262.1				
			237	240.1			272	273.9	276.2		*269*
239	**238**	**238.2**	239	**241.1**	**238.2**	**238.4**			280.8		
		244.8	245	246.3	248.9		290.2	291.6	295.3	*288.7*	289.7
			261	**260.8**	*257.9*		304.1				298.3
				271.6			320.3	*314.5*	**323.6**	**318.9**	320
		278.2			276.6				**329.4**		
				286.5		284	337.2	338	**341.3**	**338.4**	**335.7**
302.5	**298**	301.5	302	**303.2**	300.7	*300.5*			*345.6*		
		323.3				320.1			*358.1*		
		327.7			**328.9**		373.4	377.7	**368.5**		
				340.3			381.5	*383.4*	388.7	**377.6**	*382.9*
				342.9			393.6	395.1	**399.6**	**395.3**	**394.5**
343.9	**344**	**343.5**	343	**345.4**	**339.9**	**345.3**	406.3	407	**412.1**	**404.4**	*404.7*
				374			428.9	431.2	430.2	427.8	
385.2		383.8		**381**	**381.7**	*387*		434.9	**436.3**		
402.8	407	402.1	402	**402.6**	**399**	**407.6**	445.8	447.3	**452.9**	**444.4**	**443.6**
422.7	422	421.7	422	424.2	418.5		462.7	466.3	**469.3**	*463.7*	
445.9	447	445.5	446	*445.4*	443.2	444.3	476.1	476.5	**480.2**	**475.6**	**475.3**
				448			493.8	496.8	**499.4**	*493.9*	488.5
		458.8	457	458.6	*459.9*		511.7			*507.6*	
		472.9		*478.7*	*476.4*		533.6		528.9	*525.4*	
			487	*488.3*			557.5	559.8	**562.9**	**557.1**	**557.8**
527	522	524.9	519	**528.1**	**521**	**523.5**	565.6		**570.9**	*569.8*	
					533.7		587.8	578.7	583.3		*581*
540.8	543		540	541.9	544.7	*538*			*600.9*		598.5
553.5	551	551.5	553	554.5		**550.2**			*607.2*		
581	582	580.3	580	**582.1**	**578.5**	574.9			**620.4**	616.1	*616*
		594.5			*593.9*		704.1	704.1	708.4	706.9	701.3
664.8	**665**	**663.8**	665	**664.9**	*662.1*	**661.8**	716.5	**716.2**	**719.6**	**716.5**	**716**
687.1	**685**	**686.1**	687	**687.7**	*684.2*	**684.2**	725.3				
						736.1	735.2	**736.1**	**739.8**	**735.9**	**735.3**
	751	750.7		752.7	*753.3*	**753.9**			*780.1*		
853.2	856	851.1		**851**	**852.9**	848.7			*814*		
			886				847	851.9	**856.1**		855.8
927.9	**931**	926.6	927	929.6	929.7	929.3	873.5	*864.5*		*861.7*	865.4
936.5		935.2	937		938.6	*940.9*	887.6	888.9	**893.1**	893.8	893.2
1013.2	**1013**	**1011.3**	1014				924.1	924.7			
1034.7	**1035**	**1032.9**	1034				963.6	955.3	969.5	*969.4*	*970*
							1030.2				
							1056.5	**1055.5**			
							1075	**1073.3**			
							1092.8	**1093.3**			

Note: Strong peaks are in bold font; weak peaks are in italic font; intermediate peaks are in normal font.

is progressively dissolved into Ca-rich clinopyroxene and garnet (Akaogi and Akimoto 1977; Irifune and Ringwood 1987; Brey et al. 2008). Thus it is important to evaluate the phase transition pressures of OEN for various potential mantle compositions. We thus chose to study two natural Fe-bearing samples representative of possible upper mantle compositions, and a composition near the MgSiO₃ end-member for the sake of comparison with prior work and calibration.

In this paper, we report the results of in situ high-pressure room-temperature Raman experiments with several chemically distinct samples loaded together in a sample chamber of a diamond-anvil cell (DAC) to investigate the effects of compositional variations in natural orthoenstatite on the newly discovered *Pbca* → *P2₁/c* phase transition.

SAMPLE DESCRIPTION AND EXPERIMENTAL METHODS

Natural orthenstatite samples from three different locations and with different chemical compositions were used in this study: (1) near end-member MgSiO₃ orthoenstatite from Zabargad Island, Egypt; (2) Al-free Fe-bearing orthoenstatite from the Morogoro Region, Tanzania; (3) Al-rich Fe,Ca-bearing orthoenstatite from Kilbourne Hole, New Mexico. Samples of high optical quality were polished into plate-like samples of ~20 μm thickness using Al₂O₃ abrasive film (down to 0.3 μm grain size). All samples were scratch-free under optical examination, and were cut into pieces approximately 20–60 μm wide for compositional analysis and DAC loading.

The chemical composition of each sample was analyzed using a JXA 8100 electron microprobe at Nanjing University. All elemental analyses were performed using an accelerating potential of 15 kV, a beam current of 20 nA, and a beam 1 μm in diameter. Element peaks and backgrounds were measured with counting times of 20 and 10 s, respectively. A ZAF routine correction was used in the data reduction. Hornblende was used as the standard for all the measured elements, yielding

TABLE 2. Pressure dependence of the Raman frequencies for all three samples

| OEN, $v = v_0 + a \times P + b \times P \times 10^2$ | | | | | | | | | | | |
| Zabg, near pure MgSiO$_3$ | | | | Tan, Fe-bearing Al-free OEN | | | | KBH, Fe,Al-bearing OEN | | | |
v_0	a	b	R^2	v_0	a	b	R^2	v_0	a	b	R^2
137.4(10)	**5.2(5)**	**−38.8(41)**	**0.954**	155.7(5)	0.8(2)	4.0(12)	0.989	*151.4(10)*	*1.3(3)*	*−0.3(17)*	*0.969*
170.2(3)	**2.1(1)**	**−5.4(7)**	**0.993**	169.3(6)	1.6(2)	−1.6	0.985	160.0(9)	0.3(2)	3.5(11)	0.925
190.1(9)	2.1(2)	−6.0(11)	0.981	**197.1(5)**	**0.4(2)**	**0.9(11)**	**0.909**	169.7(5)	2.0(1)	−5.3(5)	0.98
196.5(10)	1.6(3)	−4.0(16)	0.951	190.9(36)	6.0(8)	−21.2(42)	0.972	**193.7(7)**	**1.4(2)**	**−1.9(9)**	**0.958**
201.1(19)	3.8(7)	−19.8(50)	0.847	**238.2(5)**	**1.7(2)**	**−3.7(11)**	**0.986**	**238.4(4)**	**1.7(1)**	**−3.8(5)**	**0.986**
208.3(9)	**3.0(2)**	**−4.5(14)**	**0.992**	248.9(13)	0.0(4)	10.2(28)	0.936	284.0(7)	2.0(1)	−2.9(7)	0.985
240.1(6)	**1.6(2)**	**−2.7(12)**	**0.976**	*257.9*	*3.4(2)*	*−3.6(17)*	*0.997*	*300.5(34)*	*1.0(8)*	*8.0(50)*	*0.869*
241.1(8)	**2.9(2)**	**−7.3(15)**	**0.989**	**276.6(9)**	**3.5(2)**	**−10.4(14)**	**0.984**	320.1(9)	4.5(2)	−5.7(10)	0.993
246.3(10)	3.9(3)	−10.1(17)	0.989	300.7(6)	2.0(2)	−2.7(15)	0.99	**345.3(6)**	**6.2(1)**	**−10.7(7)**	**0.998**
260.8(7)	**3.9(2)**	**−6.7(13)**	**0.995**	328.9(11)	2.8(3)	2.5(18)	0.994	387.0(68)	1.4(33)	14.4(226)	0.922
271.6(61)	5.3(13)	−19.2(67)	0.853	339.9(12)	6.8(4)	−12.6(27)	0.995	**407.6(6)**	**3.9(1)**	**−7.8(6)**	**0.995**
286.5(7)	**2.8(2)**	**−5.5(11)**	**0.993**	381.7(8)	3.7(3)	−3.0(19)	0.994	444.3(11)	2.5(2)	−0.4(13)	0.976
303.2(5)	**2.6(1)**	**−4.6(9)**	**0.994**	399.0(10)	5.4(3)	−14.4(24)	0.992	**523.5(7)**	**2.7(2)**	**−0.4(9)**	**0.991**
342.9(119)	*3.6(21)*	*−7.2(93)*	*0.947*	418.5(18)	2.3(7)	3.5(53)	0.972	*538.0(9)*	*1.1(5)*	*8.7(29)*	*0.999*
340.3(81)	*6.4(15)*	*−23.6(69)*	*0.893*	443.2(7)	2.8(2)	−3.5(18)	0.991	**550.2(8)**	**2.7(2)**	**−0.7(10)**	**0.989**
345.4(11)	**6.9(3)**	**−12.2(22)**	**0.996**	459.9(16)	2.0(7)	1.1(52)	0.961	574.9(11)	2.5(2)	−2.8(14)	0.971
374.0(24)	*6.1(6)*	*−13.7(39)*	*0.979*	476.4(14)	5.5(4)	−11.4(26)	0.988	**661.8(4)**	**3.8(1)**	**−3.3(6)**	**0.998**
381.0(32)	**6.2(10)**	**−13.1(64)**	**0.947**	521.0(6)	3.1(2)	−1.0(14)	0.996	**684.2(5)**	**3.9(1)**	**−5.5(6)**	**0.997**
402.6(9)	**5.3(3)**	**−12.8(17)**	**0.994**	*533.7(28)*	*2.2(10)*	*4.5(71)*	*0.925*	736.1(42)	3.4(13)	−12.2(72)	0.802
424.2(43)	2.9(15)	−1.7(106)	0.8	544.7(20)	4.0(6)	−6.8(42)	0.962	**753.9(13)**	**2.6(3)**	**3.4(16)**	**0.985**
445.4(68)	1.1(14)	8.0(68)	0.978	**578.5(4)**	**2.0(1)**	**−0.8(9)**	**0.995**	848.7(9)	1.9(2)	5.7(11)	0.99
448.0(9)	2.4(3)	0.4(19)	0.986	*593.9(9)*	*3.5(4)*	*−8.4(29)*	*0.991*	929.3(8)	4.0(2)	−4.3(10)	0.993
458.6(17)	3.1(5)	−1.0(34)	0.965	***662.1(9)***	***4.0(3)***	***−3.3(21)***	***0.994***	*940.9(38)*	*5.7(10)*	*−6.3(64)*	*0.974*
478.7(22)	*2.3(5)*	*1.8(29)*	*0.983*	*684.2(5)*	*3.8(2)*	*−4.1(12)*	*0.997*				
488.3(12)	*3.4(4)*	*1.3(24)*	*0.99*	*753.3(20)*	*2.6(8)*	*4.8(72)*	*0.967*				
528.1(11)	**2.1(3)**	**3.5(23)**	**0.982**	*852.9(16)*	*1.1(5)*	*9.1(37)*	*0.963*				
541.9(5)	1.1(2)	10.1(13)	0.997	929.7(19)	3.5(5)	−0.2(29)	0.993				
554.5(18)	2.3(5)	2.9(36)	0.96	938.6(22)	5.7(5)	−5.8(32)	0.995				
582.1(6)	**2.0(2)**	**−0.3(11)**	**0.992**								
664.9(8)	**4.0(3)**	**−3.8(17)**	**0.994**								
687.7(7)	**4.0(2)**	**−5.6(13)**	**0.996**								
752.7(12)	3.2(4)	1.7(25)	0.989								
851.0(11)	**1.2(3)**	**8.4(22)**	**0.979**								
929.6(8)	3.7(2)	−2.1(15)	0.995								

Note: Strong peaks are in bold font; weak peaks are in italic font; intermediate peaks are in normal font.

(Table extended on next page)

results as follows: Zabargad Island (Zabg) (Mg$_{0.994}$Fe$_{0.002}$Al$_{0.004}$)$_2$(Si$_{0.996}$Al$_{0.004}$)$_2$O$_6$, or En$_{99}$Fs$_0$Di$_0$MgTs$_1$; Tanzania (Tan) (Mg$_{0.897}$Fe$_{0.097}$Ca$_{0.004}$Al$_{0.002}$)$_2$(Si$_{0.996}$Al$_{0.002}$)$_2$O$_6$, or En$_{89}$Fs$_{10}$Di$_1$MgTs$_0$; and Kilbourne Hole (KBH) (Mg$_{0.835}$Fe$_{0.090}$Ca$_{0.020}$Al$_{0.055}$)$_2$ (Si$_{0.945}$Al$_{0.055}$)$_2$O$_6$, or En$_{76}$Fs$_9$Di$_4$MgTs$_{11}$, where En indicates the Mg$_2$Si$_2$O$_6$ component, Fs is Fe$_2$Si$_2$O$_6$, Di is CaMgSi$_2$O$_6$, and MgTs is (MgAl)(SiAl)O$_6$.

High-pressure experiments were performed with a membrane-type diamond-anvil cell for precise pressure control (Chervin et al. 1995). Rhenium metal gaskets with an initial thickness of 250 μm were pre-indented to 0.070 mm using 500 μm culet, ultralow-fluorescence diamond anvils. A 250 μm diameter hole in the gasket formed the sample chamber. Three different plate-like samples (maximum ~60 μm width) and several ruby spheres were loaded together in the diamond-anvil cell sample chamber (Fig. 1). An alcohol mixture (methanol:ethanol = 4:1) was loaded as a pressure-transmitting medium. A heat gun was used to warm the chamber (up to 60 °C) to help relax differential stresses. Pressure was determined from ruby fluorescence (Mao et al. 1986) before and after the Raman experiment at each pressure; the maximum pressure difference from the two readings was 0.14 GPa or less. Maximum stress differentials were obtained during decompression runs.

In situ high-pressure single-crystal Raman spectroscopy experiments were carried out at Ecole Normale Supérieure de Lyon. Raman spectra were obtained using a multichannel Raman microprobe (LabRam HR800 from DILOR) equipped with a confocal microscope configuration that enhances the signal-to-noise ratio by eliminating most of the parasitic light from sample and diamond fluorescence. Experiments were conducted in a backscattering geometry with a Mitutoyo objective that focused the incident laser spot to less than 2 μm in diameter. The scattered Raman light is focused through a 100 μm slit into a spectrograph equipped with a 1800 gr/mm grating and analyzed by a CCD detector, giving a resolution of approximately 2.5 cm⁻¹ (Auzende et al. 2004). The accumulation times for Raman spectra were typically 60–120 s over the spectral region from 100 to 1250 cm⁻¹. Precision on Raman peak position is typically 0.2 cm⁻¹ (2σ) for strong peaks, accuracy is 1 cm⁻¹ with full-width at half maximum (FWHM) about 0.5–1 cm⁻¹. For weak peaks and overlapped peaks, the peak position uncertainty is larger, but still within 2 cm⁻¹. The 514.5 line of an argon ion laser was used as an excitation source at an output power ranging from 500 to 1500 mW. Only 5 to 10% of this power reaches the sample, due to absorption or reflection from the optical elements and diamonds in the optical path.
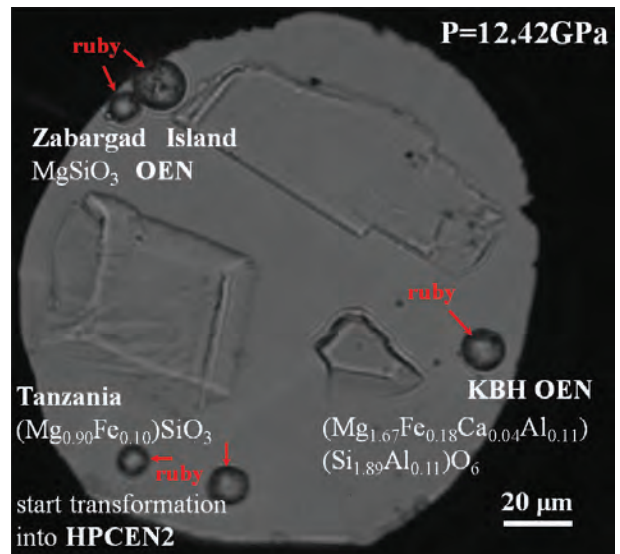

FIGURE 1. Diamond-anvil cell sample chamber. (Color online.)

TABLE 2.—*EXTENDED*

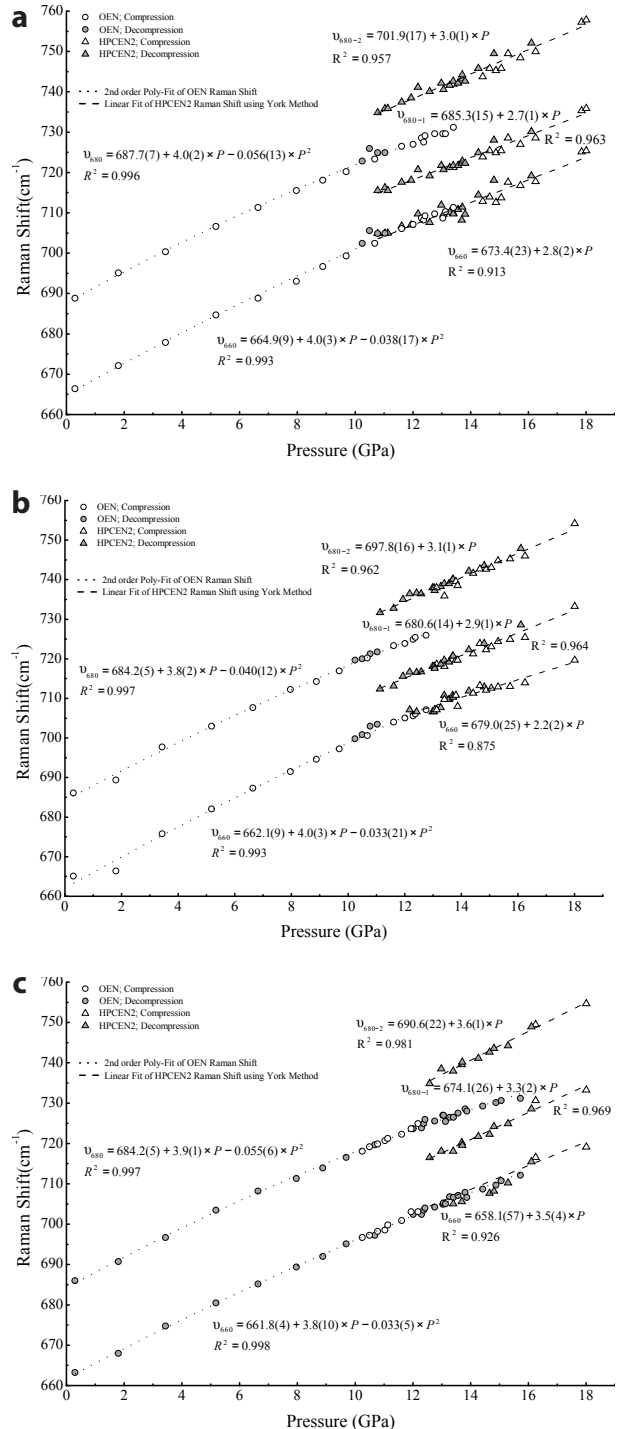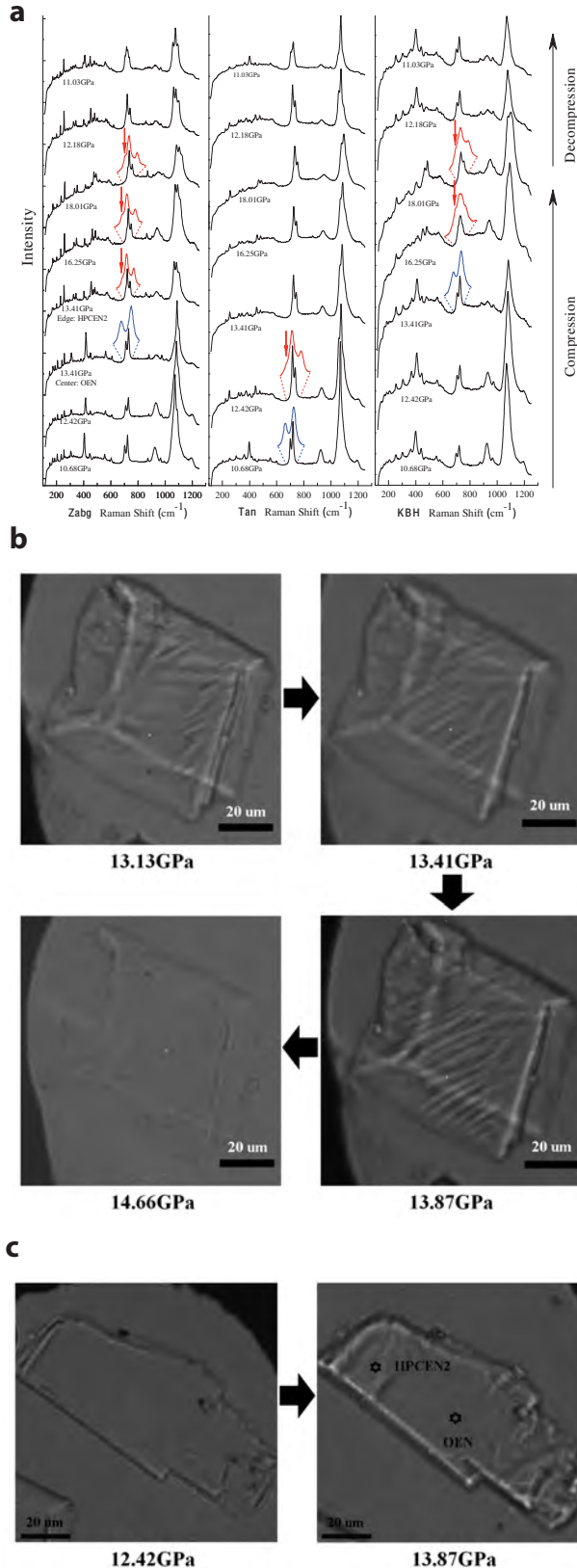| HPCEN, $v = v_0 + a \times P$ | | | | | | | | |
| ZABG, near pure MgSiO$_3$ | | | TAN, Fe-bearing Al-free | | | KBH, Fe,Al-bearing | | |
v_0	a	R^2	v_0	a	R^2	v_0	a	R^2
157.8(7)	**0.8(1)**	**0.926**	181.5(15)	1.1(1)	0.818	202.6(22)	1.7(2)	0.919
169.4(7)	*0.8(1)*	*0.919*	**211.0(7)**	**1.0(1)**	**0.938**	**235.0(11)**	**1.3(1)**	**0.963**
191.6(7)	**0.6(1)**	**0.828**	**237.9(8)**	**1.1(1)**	**0.932**	248.4(45)	1.6(3)	0.805
215.3(9)	**1.0(1)**	**0.895**	*268.3(31)*	*1.6(2)*	*0.724*	*257.1(41)*	*2.6(3)*	*0.902*
241.8(7)	**1.0(1)**	**0.945**	**300.4(10)**	**1.5(1)**	**0.938**	*191.2(219)*	*8.6(15)*	*0.938*
249.9(19)	1.4(1)	0.805	**315.4(16)**	**1.8(1)**	**0.905**	298.5(25)	1.7(2)	0.909
256.7(13)	1.6(1)	0.915	**338.1(20)**	**2.4(1)**	**0.923**	309.5(24)	2.1(2)	0.936
255.5(19)	2.0(1)	0.902	**343.9(16)**	**2.7(1)**	**0.951**	*360.8(66)*	*1.8(5)*	*0.725*
273.4(17)	1.8(1)	0.891	**371.2(11)**	**1.9(1)**	**0.957**	**370.6(13)**	**1.9(1)**	**0.977**
305.3(10)	**1.5(1)**	**0.935**	**364.8(17)**	**3.2(1)**	**0.96**	*365.9(98)*	*3.1(6)*	*0.849*
310.2(16)	**1.5(1)**	**0.876**	396.6(26)	2.5(2)	0.868	**397.5(50)**	**3.7(3)**	**0.913**
319.8(13)	**1.7(1)**	**0.93**	398.6(29)	3.7(2)	0.923	**450.7(11)**	**2.0(1)**	**0.983**
312.8(56)	*2.6(4)*	*0.788*	433.4(23)	2.4(2)	0.948	438.7(52)	4.0(4)	0.933
339.8(35)	*1.5(2)*	*0.793*	**451.9(11)**	**1.9(1)**	**0.958**	**516.1(23)**	**3.3(2)**	**0.977**
342.6(22)	*2.8(2)*	*0.957*	*457.6(18)*	*2.9(1)*	*0.956*	551.7(37)	2.3(2)	0.949
351.6(30)	*3.0(2)*	*0.936*	*473.8(42)*	*2.7(3)*	*0.913*	571.1(45)	2.2(3)	0.855
371.9(19)	**2.2(1)**	**0.905**	*478.5(43)*	*3.8(3)*	*0.927*	598.5(27)	1.4(2)	0.847
374.3(36)	**3.0(3)**	**0.856**	**524.3(22)**	**2.6(2)**	**0.916**	658.1(57)	3.5(4)	0.926
401.2(17)	2.3(1)	0.929	*545.8(47)*	*1.9(3)*	*0.625*	**674.1(26)**	**3.3(2)**	**0.969**
407.6(27)	**2.3(2)**	**0.843**	592.1(17)	1.9(1)	0.908	**690.6(22)**	**3.6(1)**	**0.981**
423.9(46)	**2.3(3)**	**0.644**	679.0(25)	2.2(2)	0.875	810.2(47)	3.7(3)	0.922
441.7(20)	**2.2(1)**	**0.903**	**680.6(15)**	**2.9(1)**	**0.964**	*841.1(23)*	*1.9(2)*	*0.982*
456.8(15)	**1.9(1)**	**0.916**	**697.8(16)**	**3.1(1)**	**0.962**	*844.7(24)*	*3.9(2)*	*0.988*
463.9(22)	**2.8(2)**	**0.923**	*840.8(29)*	*1.7(2)*	*0.706*	*947.7(21)*	*1.8(1)*	*0.935*
489.7(35)	3.1(3)	0.869	850.4(54)	3.5(4)	0.911			
528.5(28)	**2.8(2)**	**0.878**	*937.0(47)*	*2.6(3)*	*0.844*			
534.4(23)	**2.9(2)**	**0.92**						
550(23)	2.7(2)	0.912						
582.5(33)	*1.5(2)*	*0.791*						
574.6(36)	*2.6(3)*	*0.896*						
595.1(18)	**2.0(1)**	**0.901**						
673.4(23)	2.8(2)	0.913						
685.3(15)	**2.7(1)**	**0.963**						
701.9(17)	**3.0(1)**	**0.957**						
738.8(24)	*3.3(2)*	*0.962*						
782.9(36)	*2.5(3)*	*0.86*						
824.9(13)	**2.5(1)**	**0.963**						
846.4(23)	1.4(2)	0.764						
853.8(22)	**3.1(2)**	**0.937**						
939.6(27)	2.4(2)	0.858						

RESULTS

High-pressure Raman data were collected at 47 different pressures between 0.30(1) and 18.01(2) GPa in several compression and decompression cycles. The number of Raman-active modes in orthoenstatite is predicted to be 120 (Ferraro 1975). However, the number of observed Raman bands is smaller in any given run due to the weak intensity and/or overlap of many bands, and the strong orientation dependence of intensity. Because the edge filter used to cut off Rayleigh scattering limits the measured Raman shifts to above 100 cm^{-1}, we were not able to observe the lowest frequency bands of OEN. Another limitation included the overlap of the strong methanol ethanol C-O stretching band at ~1030 cm^{-1} with OEN and HPCEN2 peaks near that frequency shift.

We consistently observed 34 bands in Zabg OEN, 40 bands in Zabg HPCEN2; 28 bands in Tan OEN, 26 bands in Tan HPCEN2; 23 bands in KBH OEN, 24 bands in KBH HPCEN2. The results are listed in Tables 1 and 2. Our observations are in good agreement with previous results (Lin 2003; Chopelas 1999; Huang et al. 2000; Stalder et al. 2009; Reynard et al. 2008; Zucker and Shim 2009). Small discrepancies were due to crystal orientation effects, overlap of peaks, and weak intensities of some peaks.

Typical Raman spectra of OEN and HPCEN2 for all three samples are shown in Figure 2a. In the low-frequency range, the transition is characterized by the occurrence of HPCEN2 peaks (e.g., for Zabg OEN at 12.5 GPa, 199.5, 228.3, and 341.9 cm^{-1}), with fading OEN peaks (206.6, 238.5, 210.5, 218.1, 308.2, and 312.7 cm^{-1}). The single most significant characteristic of this transition is splitting of the strong 660–680 cm^{-1} doublet into a triplet (Fig. 3), accompanied by a change in the relative intensities of the peaks. The 660–680 cm^{-1} doublet is assigned to the Si-O-Si bending mode of the tetrahedral chains. A change in the number of peaks in that region indicates a change in the number of symmetrically distinct tetrahedral chains, which is diagnostic of the phase transition (Chopelas and Boehler 1992; Ross and Reynard 1999). The observation of an increase from two to three peaks is consistent with X-ray structural refinements of the HPCEN2 phase, which indicate that the number of distinct tetrahedral (T) chains doubles across the OEN-HPCEN2 transition (Fig. 4). In detail, the A site T-chain in the OEN structure splits into two T-chains with the O3-O3-O3 angle changing from 160.71(16)° to 148.44(79)° and 216.61(77)°. The B site T-chain in OEN undergoes a change in O3-O3-O3 angle from 135.44(15)° to 131.94(72)° and 133.13(49)° (Zhang et al. 2012). The large change of angle in the A chain is related to the split of the Raman doublet, whereas the change for the B chain is so small that the associated Raman peak splitting cannot be resolved, thus yielding a spectral triplet instead of a quadruplet. For similar reasons, the doublet of OEN transforms to a single

a

b

c

a

$$\upsilon_{680-2} = 701.9(17) + 3.0(1) \times P$$
$$R^2 = 0.957$$

$$\upsilon_{680-1} = 685.3(15) + 2.7(1) \times P$$
$$R^2 = 0.963$$

$$\upsilon_{680} = 687.7(7) + 4.0(2) \times P - 0.056(13) \times P^2$$
$$R^2 = 0.996$$

$$\upsilon_{660} = 673.4(23) + 2.8(2) \times P$$
$$R^2 = 0.913$$

$$\upsilon_{660} = 664.9(9) + 4.0(3) \times P - 0.038(17) \times P^2$$
$$R^2 = 0.993$$

b

$$\upsilon_{680-2} = 697.8(16) + 3.1(1) \times P$$
$$R^2 = 0.962$$

$$\upsilon_{680-1} = 680.6(14) + 2.9(1) \times P$$
$$R^2 = 0.964$$

$$\upsilon_{680} = 684.2(5) + 3.8(2) \times P - 0.040(12) \times P^2$$
$$R^2 = 0.997$$

$$\upsilon_{660} = 679.0(25) + 2.2(2) \times P$$
$$R^2 = 0.875$$

$$\upsilon_{660} = 662.1(9) + 4.0(3) \times P - 0.033(21) \times P^2$$
$$R^2 = 0.993$$

c

$$\upsilon_{680-2} = 690.6(22) + 3.6(1) \times P$$
$$R^2 = 0.981$$

$$\upsilon_{680-1} = 674.1(26) + 3.3(2) \times P$$
$$R^2 = 0.969$$

$$\upsilon_{680} = 684.2(5) + 3.9(1) \times P - 0.055(6) \times P^2$$
$$R^2 = 0.997$$

$$\upsilon_{660} = 658.1(57) + 3.5(4) \times P$$
$$R^2 = 0.926$$

$$\upsilon_{660} = 661.8(4) + 3.8(10) \times P - 0.033(5) \times P^2$$
$$R^2 = 0.998$$

▲ **FIGURE 3.** Raman frequency shifts of the 660–680 cm⁻¹ doublet/triplet as a function of pressure. (**a**) Zabargad Island, Egypt. (**b**) Morogoro Region, Tanzania. (**c**) Kilbourne Hole, New Mexico.

◄ **FIGURE 2.** (**a**) Selected Raman spectra of OEN and HPCEN2 for all three samples at high pressures. The 660–680 cm⁻¹ doublet-to-triplet changes for each of the samples are indicated with red arrows. (**b**) Optical observation of the OEN → HPCEN2 phase transition in the mixed phase region for sample Tan. (**c**) Optical observation of the OEN → HPCEN2 phase transition in the mixed phase region for sample Zabg. (Color online.)

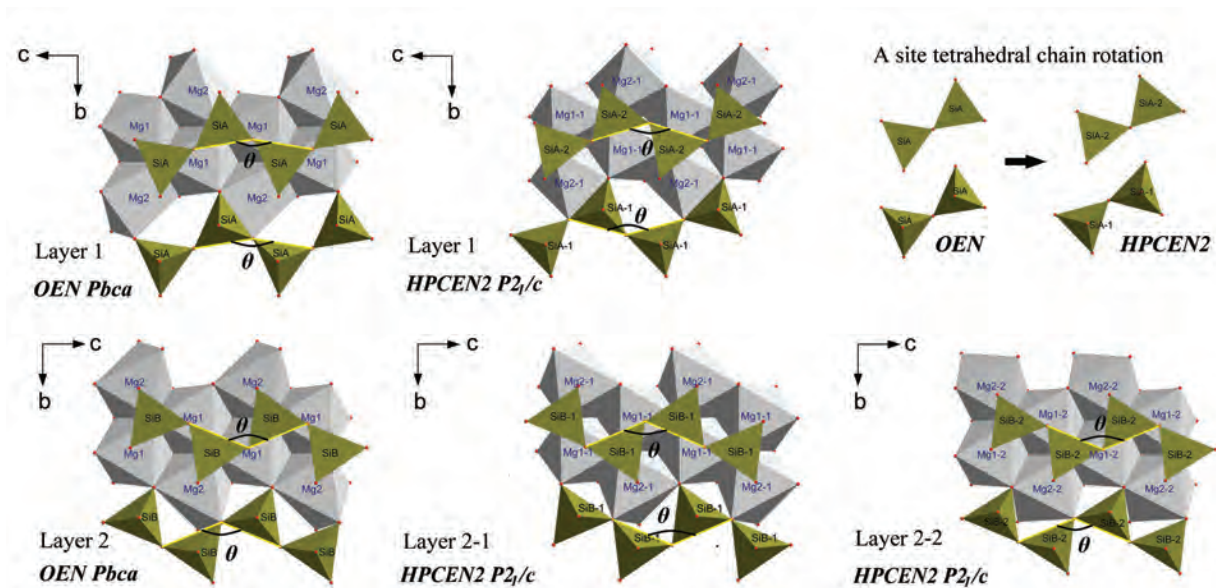**FIGURE 4.** Structural change associated with the OEN → HPCEN2 phase transition. O3-O3-O3 angle is marked as θ in the figure. The largest change of θ occurs on the A site tetrahedral that is shown on the top right. (Color online.)

peak in the same frequency region upon transition to HPCEN with space group *C*2/*c* (Chopelas and Boehler 1992; Ross and Reynard 1999). These clear spectral differences makes Raman spectroscopy an efficient tool to differentiate OEN polymorphs from each other (Lin 2004).

DISCUSSION AND CONCLUSION

For all three OEN samples, peak splitting associated with the *Pbca* → *P*2$_1$/*c* phase transition was observed. Evidence for a *C*2/*c* phase, which was claimed to be the stable high-pressure phase above ~7–9 GPa (Angel et al. 1992), was not observed over the pressure range of the present experiments. We were able to observe the formation of domains as the transition proceeded (e.g., Figs. 2b and 2c). There are two distinctive characteristics of these domains. First, they developed upon initiation of the transition, and disappeared after the transition was completed (e.g., Fig. 2b). All samples were single crystals by optical examination before initiation and after completion of the high-pressure transition. Second, the formation of *P*2$_1$/*c* phase domains started from edges of the sample and progressed toward the center (e.g., Zabg OEN, Fig. 2c). Edges may have a high density of crystal defects that act as nucleation sites for the new phase.

The onset pressure of the *Pbca* → *P*2$_1$/*c* transition (P_{Tr}) is different for the three samples. For near Mg-end-member Zabg OEN, P_{Tr} is between 13.13(11)–13.41(8) GPa on compression, and between 11.03(1)–11.13(11) GPa on decompression. For near-Al-free, Fe-bearing Tan OEN, P_{Tr} was constrained between 12.38(3)–12.42(4) and 11.03(1)–11.13(11) GPa in compression and decompression cycles, respectively. For Al-rich, Ca,Fe-bearing KBH OEN, P_{Tr} was constrained as between 15.73(12)–16.25(14) and 12.18(1)–12.58(1) GPa during compression and decompression, respectively. A comparison between Zabg OEN and Tan OEn indicates that 10 mol% Fe content decreased the onset pressure of the initial formation of HPCEN2 by ~1 GPa;

however, the comparison between KBH and Tan OEN is more complex, including differences in both Al and Ca contents. KBH OEN contains 0.22 Al per formula unit (pfu, based on 6 O atoms), which is 27.5 times more than in Tan OEN. The Ca content of KBH OEN is 0.040 pfu, which is 5 times more than in Tan OEN. Considering the fact that the Fe contents are very close to each other, the presence of 0.212 pfu more Al and 0.032 pfu more Ca increased the onset pressure of the initial formation of HPCEN2 by over 3 GPa. Notably, it seems that the transition pressure during decompression is less sensitive to composition – ~10 mol% Fe does not change decompressional transition pressure while 0.212 pfu more Al and 0.032 pfu more Ca increased it only by about 1 GPa.

Increased repulsion between the M2 site cation and A-site Si was believed to be a key factor in determining the topology of pyroxene structures at higher pressure. Iron prefers M2 sites over the M1 sites as suggested from the structure refinement for both OEN and HPCEN2 (e.g., Zhang et al. 2012). The substitution of Fe atoms into the structure results in a larger M2 site, thus giving the Si-O tetrahedral chains more spatial flexibility, and making this *Pbca* → *P*2$_1$/*c* transition, which is characterized by tetrahedral rotation, easier to occur at lower pressure. Similar qualitative arguments for the effects of Ca and Al are less obvious, because the effects of these two elements cannot be decoupled in this experiment. We do not rule out the possibility that a small amount of Ca might have a significant effect on the transition pressure, as it has a resolvable effect on the OEN structure (Nestola and Tribaudino 2003). Additional experiments would be needed to determine pure Ca or Al effects using synthetic samples. However, the much greater abundance of Al over Ca in KBH OEN suggests to us that the enrichment of Al is the primary cause of the increase in the onset of P_{Tr}. The case of Al substitution into the crystal structure is complicated since it involves a coupled substitution mechanism, with half

the Al atoms occupying the tetrahedral A site substituting for Si, and half occupying the M1 sites substituting for Mg, resulting in a Mg-Tschermaks component in the KBH OEN. In this case, two competing processes, due to Al occupying two polyhedral sites, will be operative. Although the individual effects of these two substitutions are not resolved by the present experiments, net effect is to increase the phase transition pressure.

In the upper mantle, the Fe content in OEN does not change much with depth, whereas Ca and Al contents decrease with increasing depth (Akaogi and Akimoto 1977; Irifune and Ringwood 1987; Brey et al. 2008). Al and Ca will be enriched in Ca-rich clinopyroxene and garnet in comparison to OEN. Thus, in the 300–450 km depth range where this phase transition might occur, the composition of OEN is probably between San Carlos OEN (Zhang et al. 2012) and Tan OEN, but likely closer to Tan OEN. Neglecting thermal effects, our results suggest a transition depth of about 350–400 km (if the OEN has not yet completely dissolved into the garnet structure), just above the 410 km discontinuity. Additional studies, including high-temperature measurements of the stability of HPCEN2, and single-crystal elasticity measurements, will be required to obtain better estimates of the depth at which the OEN-HPCEN2 transition occurs in the mantle, and its seismic signature.

REFERENCES CITED

Akaogi, M. and Akimoto, S. (1977) Pyroxene-garnet solid-solution equilibria in the systems $Mg_4Si_4O_{12}$-$Mg_3Al_2Si_3O_{12}$ and $Fe_4Si_4O_{12}$-$Fe_3Al_2Si_3O_{12}$ at high pressures and temperatures. Physics of the Earth and Planetary Interiors, 15, 90–106.

Angel, R.J., Chopelas, A., and Ross, N.L. (1992) Stability of high-density clinoenstatite at upper-mantle pressures. Nature, 358, 322–324.

Auzende, A.-L., Daniel, I., Reynard, B., Lemaire, C., and Guyot, F. (2004) High-pressure behaviour of serpentine minerals: a Raman spectroscopic study. Physics and Chemistry of Minerals, 31, 269–277.

Brey, G.P., Bulatov, V.K., and Girnis, A.V. (2008) Geobarometry for peridotites: experiments in simple and natural systems from 6 to 10 GPa. Journal of Petrology, 49, 3–24.

Chai, M., Brown, J.M., and Slutsky, L.J. (1997) The elastic constants of an aluminous orthopyroxene to 12.5 GPa, Journal of Geophysical Research, 102(B7), 14779–14785.

Chervin, J.C., Canny, B., Besson, J.M., and Pruzan, P. (1995) A diamond anvil cell for IR microspectroscopy. Review of Scientific Instruments, 66, 2595–2598.

Chopelas, A. (1999) Estimates of mantle relevant Clapeyron slopes in the $MgSiO_3$ system from high-pressure spectroscopic data. American Mineralogist, 84, 233–244.

Chopelas, A. and Boehler, R. (1992) Raman spectroscopy of high pressure $MgSiO_3$ phases synthesized in a CO_2 laser heated diamond anvil cell: Perovskite and clinopyroxene. In Y. Syono and M.H. Manghnani, Eds., High-Pressure Research: Application to Earth and Planetary Sciences, Geophysical Monograph, 67, 101–108. American Geophysical Union, Washington, D.C.

Ferraro, J.R. (1975) Factor group analysis for some common minerals. Applied Spectroscopy, 29, 418–421.

Huang, E., Chen, C.H., Huang, T., Lin, E.H., and Xu, Ji-an. (2000) Raman spectroscopic characteristics of Mg-Fe-Ca pyroxenes. American Mineralogist, 85, 473–479.

Irifune, T. and Ringwood, A.E. (1987) Phase transformations in primitive MORB and pyrolite compisitions to 25 GPa and some geophysical implications. In M.H. Manghnani and Y. Syono, Eds., High-Pressure Research in Mineral Physics, 39, 231–242. Geophysical Monograph, American Geophysical Union, Washington, D.C.

Kung, J., Li, B., Uchida, T., Wang, Y., Neuville, D., and Liebermann, R.C. (2004) In situ measurements of sound velocities and densities across the orthopyroxene → high-pressure clinopyroxene transition in $MgSiO_3$ at high pressure. Physics of Earth and Planetary Interiors, 147, 27–44.

Lin, C.-C. (2003) Pressure-induced metastable phase transition in orthoenstatite ($MgSiO_3$) at room temperature: a Raman spectroscopic study. Journal of Solid State Chemistry, 174, 403–411.

——— (2004) Pressure-induced polymorphism in enstatite ($MgSiO_3$) at room temperature: clinoenstatite and orthoenstatite. Journal of Physics and Chemistry of Solids, 65, 913–921.

Mao, H.K., Xu, J., and Bell, P.M. (1986) Calibration of the ruby pressure gauge to 800 kbar under quasi-hydrostatic conditions. Journal of Geophysical Research, 91, 4673–4676.

Morimoto, N. and Koto, K. (1969) The crystal structure of orthoenstatite. Zeitschrift für Kristallographie, 129, 65–83.

Morimoto, N., Appleman, D.E., and Evans, H.T. Jr. (1960) The crystal structures of clinoenstatite and pigeonite. Zeitschrift für Kristallographie, 114, 120–147.

Nestola, F. and Tribaudino, M. (2003) The structure of Pbca orthopyroxenes along the join diopside-enstatite ($CaMgSi_2O_6$-$Mg_2Si_2O_6$). European Journal of Mineralogy, 15, 365–371.

Reynard, B., Bass, J.D., and Jackson, J.M. (2008) Rapid identification of steatite–enstatite polymorphs at various temperatures. Journal of the European Ceramic Society, 28, 2459–2462.

Ross, N.L. and Reynard, B. (1999) The effects of iron on the $P2_1/c$ to $C2/c$ transitions in (Mg,Fe)SiO_3 clinopyroxenes. European Journal of Mineralogy, 11, 585–589.

Stalder, R., Kronz, A., and Schmidt, B.C. (2009) Raman spectroscopy of synthetic (Mg,Fe)SiO_3 single crystals. An analytical tool for natural orthopyroxenes. European Journal of Mineralogy, 21, 27–32.

Zhang, J.S., Dera, P., and Bass, J.D. (2012) A new high-pressure phase transition in natural Fe-bearing orthoenstatite. American Mineraogist, 97, 1070–1074.

Zucker, R. and Shim, S.-H. (2009) In situ Raman spectroscopy of $MgSiO_3$ enstatite up to 1550 K. American Mineralogist, 94, 1638–1646.